Available online at www.sciencedirect.com

jmr&t Journal of Materials Research and Technology

journal homepage: www.elsevier.com/locate/jmrt

Original Article

Effect of particle size and morphological structure on the physical properties of $NiFe_2O_4$ for supercapacitor application

Arafat Toghan [a,c], *M. Khairy* [a,b,*], *E.M. Kamar* [b], *M.A. Mousa* [b]

[a] *Chemistry Department, College of Science, Imam Mohammad Ibn Saud Islamic University (IMSIU), Riyadh 11623, Saudi Arabia*

[b] *Chemistry Department, Faculty of Science, Benha University, Benha, Egypt*

[c] *Chemistry Department, Faculty of Science, South Valley University, Qena 83523, Egypt*

ARTICLE INFO

Article history:
Received 15 April 2022
Accepted 19 June 2022
Available online 24 June 2022

Keywords:
$NiFe_2O_4$
Activated carbon
Composite
Supercapacitor
Electrospinning

ABSTRACT

Activated carbon (AAC), $NiFe_2O_4$, and binary nanocomposites of $NiFe_2O_4$ and AAC electrodes have been prepared for supercapacitor applications. Nickel ferrite ($NiFe_2O_4$) was prepared using four different ways: electrospinning, hydrothermal, sol–gel, and green method. The samples were characterized by XRD, FT-IR, SEM, TEM, and BET techniques. The results showed the formation of the ferrite in the cubic spinel phase with different morphological structures of nanofibers, nanotubes, nanorods, and nanospheres, as well as the formation of AAC in the flake structure. The influence of synthetic methods on electrochemical properties and their applications in storage energy was studied using cyclic voltammetry (CV), galvanostatic charge/discharge (GCD), and impedance methods in a 6 M KCl electrolyte solution. The data obtained illustrated pseudo-capacitive behavior with a revisable charge/discharge property. The maximum specific capacitance for ferrite samples increased with decreasing the particle size and a capacitance value of 1130 F g^{-1} for the NiF_2O_4 nanofibers (NiF_f) sample. The AAC electrode has a specific capacitance of 432 F/g. The capacitive data of an asymmetric capacitor designed from the AAC@NiF_f composite electrode, the activated carbon (AAC), and a solid electrolyte composed of PVA and KOH were studied. The capacitor shows a specific capacitance of 135 F/g, a maximum energy density of 34.7 Wh/kg, a maximum power density of 5314 W/kg, and high cycling performance, with 88% capacitance retained over 10000 cycles.

1. Introduction

Particles with nano-size possess wonderful properties and have various imaginable applications in different fields such as electronics, sensors, fuel cells, batteries, supercapacitors, etc. [1–5]. The physical properties of the nanoparticles hang permanently on the production route [6]. The nanoparticles exhibit an excellent surface-to-volume ratio and the existence of infinite grain boundaries that dominate an elevated defect's

* Corresponding author.
E-mail address: mohkhairy@fsc.bu.edu.eg (M. Khairy).

https://doi.org/10.1016/j.jmrt.2022.06.095

density, which cause unlimited effects on their physical properties such as mechanical, optical, magnetic, electrical, and electrochemical behaviors [5]. Materials with nanoparticles submit numerous improvements in energy appliances, which involve physical interaction and chemical reactions at the surface or border zones in crystalline materials. Accordingly, the surface properties such as its roughness and the conductivity at the grain boundary play a significant task in storing energy in the nanomaterials.

At present, various effective technologies for energy storage have been explored. The supercapacitor is a forward-looking energy storing device, storing a very large electric capacitance in a very condensed arrangement, and is widely used in many electronic devices. It has several advantages such as wide operating temperature ranges, unlimited cycle life, simple charging and discharging circuit, quick charging time, and low cost [7–9]. The supercapacitor performance is managed by the electrodes, current collectors, separator, and electrolyte. The surface and electrical properties of electrodes are the main factors that principally regulate the energy storage in supercapacitors. Accordingly, a lot of works are being appointed for developing new electrode materials and advancing their electrochemical properties [10–15].

Supercapacitors are classified into two types: electric double-layer capacitors and pseudocapacitors. They have various charge storage mechanisms. In the standard electric double-layer capacitors (EDLC), there are no faradaic and redox reactions on the electrode surface, which can be deduced from the rectangular shape produced through cyclic voltammetry characterization. It is based on electrostatic effects between two electrodes with high specific surface areas per volume, such as graphene and its surrounding electrolyte. The charge is stored at the electrolyte/graphene interface through the adsorption/desorption of electrolyte ions onto the graphene surface. Due to the absence of the electrochemical reactions, the EDLC has a higher lifecycle and lower energy density than the pseudocapacitor. However, the pseudocapacitor rests on a high-speed and reversible redox reaction to store charge. Generally, conducting polymers and transition metal oxides are being counted as promise electrodes in pseudosupercapacitor owing to their different oxidation states, environmental kindliness, and large abundance [16–22]. $NiFe_2O_4$, as one of the mixed transition metal oxides, was used as an electrode in supercapacitor applications [23–26]. $NiFe_2O_4$ particles with submicron-sized made by the molten salt process showed a specific capacitance of 18.5 F g^{-1} at a scan rate of 10 mV/s [27]. But, the use of $NiFe_2O_4$ as electrode material meets limitations due to its low electrical conductivity (~$10^{-7} - 10^{-8}$ S cm^{-1}) [28]. Thus, an increase in the electrical conductivity of the $NiFe_2O_4$ is necessary to be used as electrode material. This can be done by mixing the ferrite with a conducting material with a high surface area, such as activated carbon. Soam et al. [29] synthesized ferrite/graphene nanocomposite electrode with a specific capacitance of 207 Fg^{-1} in 1 M Na_2SO_4 electrolyte. This capacitance value is about 4 times greater than the $NiFe_2O_4$ electrode.

Regarding EDLC electrode materials, activated carbon (AC) has been the preferred choice as an electrode due to its availability, porosity, good electrical conductivity, chemical stability, low cost, and high specific surface area [30]. Based on the above-mentioned properties, supercapacitors with high capacitance can be fabricated via the advantages of activated carbon and transition metal oxides with different valence states. Since the variation of the surface area of the nanomaterials with changing their morphological structure affects their storing energy. Thus, the One-dimensional nanostructured materials have advantages in energy storage due to their extraordinary porosity, huge surface area, well permeability, and speedier electron, and ion migration rates. These can excellently increase energy density, power density, and cycling performance for energy storage [31,32].

The size and shape controlling of nano ferrites is the main factor that affects their properties and subsequently their applications. We previously reported the influence of the synthetic methods of $NiFe_2O_4$, which exhibits inverse spinel structure [33], on each of the dye adsorption, optical and magnetic properties [34]. As an extension of our previously published work, the current paper was designed to study how the different morphologies of the $NiFe_2O_4$ nanoparticles (spheres, tubes, rods, and nanofibers) alter their electrochemical properties. The use of nickel ferrite as electrodes, in the form of a single or binary composite material (AAC@$NiFe_2O_4$), in fabricated supercapacitors was investigated. The nanofiber $NiFe_2O_4$@AAC electrode with the most excellent capacitance was tested to be used as a positive electrode to assemble an asymmetric supercapacitor with AAC as a negative electrode.

2. Experimental

2.1. Materials

All chemicals used were analytical grade reagents and were used without any further purification. Commercial active carbon based on coconut shell was supplied from Shanghai Active Carbons (China). De-ionized water was used through manifests all the experiments. *Tamarindus indica* seeds were provided from the local market.

2.2. Synthesis of samples

2.2.1. Preparation of modified activated carbon

AC was blended with KOH at the mass ratio of AC: KOH = 1:5 ground effectively and then heated at 1100 K in an N_2 atmosphere for 1 h. The product obtained was soaked in 0.1 M HCl aqueous solution and subsequently washed and filtered with de-ionized water up to the filtrate becomes neutral. Finally, the product was dried at 350 K for 48 h and denoted as AAC [35].

2.2.2. Synthesis of ferrite samples

Electrospinning, hydrothermal, and green methods were used to synthesize different morphological structures of $NiFe_2O_4$ samples.

2.2.3. Electrospinning method

2.2.3.1. Preparation of $NiFe_2O_4$ nanofibers (NiF_f). Firstly, an electrospun precursor was organized by mixing a mixture of 30 ml of methanol, 1.5 g of PVP, 3.0 g of $Fe(NO_3)_3.9H_2O$, 3 mL of

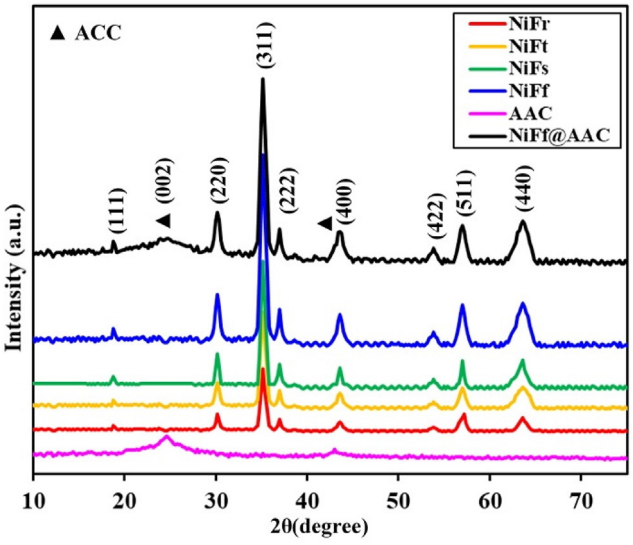

Fig. 1 – XRD of the investigated samples.

acetic acid, and 0.3 g of $Ni(CH_3COO)_2.4H_2O$, and magnetically stirred for 24 h at room temperature. Next, 6 mL of the gotten precursor was introduced into a 20 mL syringe with a 22 G stainless steel needle, joined to a high-voltage supply with a 20 kV applied voltage. The space between the needle end and the aluminum foil collector was 15 cm. The supply rate is adjusted to be 1.2 mL h^{-1} by a syringe pump. Lastly, the obtained spun fibrous were calcined at 825 K for 2 h (at a heating rate of 4 K min^{-1}) in a Muffle furnace under an air atmosphere. The sample obtained is denoted as NiF_f [36].

2.2.3.2. *Preparation of $NiFe_2O_4$ nanotubes (NiF_t).* Two grams of the as-synthesized sample NiF_f were placed in a 200 mL beaker filled with de-ionized water. After 4 h of high-speed magnetic stirring, the products were filtered and dried at 350 K for 24 h in a vacuum [36]. The sample is denoted as NiF_t.

2.2.4. *Hydrothermal method (Preparation of $NiFe_2O_4$ nanorods (NiF_r))*

Starting materials of 0.02 M $FeCl_3$ and 0.01M $NiCl_2.6H_2O$ were dissolved in 200 mL of de-ionized water. Then 2.5 M NaOH solution was added dropwise until pH of 1.5. After that, the suspended solution was transferred to a Pyrex flask (500 ml), which was sited inside an autoclave and heated at 435 K for 4 h under the stirring process. The suspended solution was washed thoroughly to release the formed salts and unreacted materials. The product was then filtered with filter papers and dried at 350 K in an oven for 4 h [37]. The sample was denoted as NiF_r.

2.2.5. *Green method*

A green method was also used to prepare the $NiFe_2O_4$ sample by mixing *T. indica* seed powder and $Fe(NO_3)_3.9H_2O$ and $Ni(NO_3)_2.6H_2O$ with a molar ratio of 2:1 (Fe: Ni) in 60 mL deionized water. The ratio of metal nitrates to the seed powder is 1:1. The reaction mixture was heated with agitation in a microwave oven (frequency of 2.54 GHz at 900 W output power) for 30 min. The obtained product was annealed at 870 °C for 4 h [38]. The sample was denoted as NiF_s.

2.2.6. *Preparation of $NiFe_2O_4$@AAC composite*

1.0 g of the prepared AAC was added to 90 mL de-ionized water in a 250 mL beaker and dispersed by sonication for 1 h; then, 2.0 g fiber $NiFe_2O_4$ (NiF_f) was inserted into the suspension with stirring for 2 h. The suspended solution was then transferred to a 250-mL Teflon-lined autoclave and heated to 400 K for 6 h. Lastly, the autoclave was placed sideways to cool to 300 K, and the gotten precipitant product was eventually washed using a large amount of deionized water, dried, and symbolized as AAC@NiF_f. The prepared sample was analyzed by the EDX technique, which displayed peaks relayed only to Ni, Fe, C, and O with weight percentages of 16.7%, 32.0%, 32.9%, and 18.4%. These outcomes agree well with the initial starting ratios of the used materials.

2.3. *Characterization methods*

The obtained samples were characterized using different techniques. The Phase analysis was performed by the XRD technique, using a Philips X′ Pert Pro Super diffractometer with Cu Kα radiation (λ = 1.54 Å) in the range of 2θ = 10-75°. A BRUCKER FT-IR spectrometer recorded the FT-IR spectra in the range of 4000–400 cm^{-1}. The synthesized sample's morphology and size were analyzed by SEM, JEOL JEM-100CXII, and TEM by JEOL-2010. The surface properties were analyzed via N_2 adsorption/desorption at 77 K by the volumetric technique via a NOVA 2200 apparatus. The pores size was calculated using BJH (Barrett-Joyner- Halenda) method from the adsorption isotherms.

The investigated electrodes' supercapacitive performance was studied at room temperature using a three-electrode cell

Table 1 – XRD, TEM, FTIR, and N_2 adsorption data of the investigated samples.

Sample	D'_{XRD} (nm)	D_{TEM} (nm)	ν_o (cm^{-1})	ν_t (cm^{-1})	Surface area (m^2/g)	Pore Size (nm)
NiF_f	20	Diam = 55 Length = several millimeters	451.3	562.5	360	5.6
NiF_t	33	Diam. = 9 Length = 230	445.3	558.1	115	4.9
NiF_r	41	Diam. = 30 Length = 150	444.3	556.4	82	4.1
NiF_s	50	35	443.9	556.2	54	3.5
AAC	45	20–40			3337	5.8
AAC@NiF_f	15	–	453.1	563.9	2570	6.4

containing the working electrode, a counter electrode (a 0.59 cm2 Pt square foil), and a reference electrode (a saturated calomel electrode, SCE) in a 6 M KCl electrolyte solution. The working electrode was prepared using a homogenous slurry of the active materials with carbon black as a conductive additive and poly(vinylidene difluoride) as a binder in a DMF solvent with a weight ratio of 8:1:1. The slurry was then coated onto FTO glass and dried under vacuum at 230 K for 24 h. The electrochemical behaviors of the prepared electrodes were analyzed on an SP 300, BioLogic potentiostat using the CV, galvanostatic charge–discharge (GCD), and EIS measurements at frequencies ranging between 10–1 and 105 Hz. An asymmetric supercapacitor (ASC) in a two-electrode setup using a Swagelok cell was also studied using the NiFf@AAC nanocomposites as an anode electrode. The AAC has used a cathode electrode and a gel electrolyte composed of PVA and KOH as the separator to demonstrate the real-world application of the prepared materials.

3. Results and discussion

3.1. XRD

The XRD patterns of all the investigated samples are shown in Fig. 1. The spectrum of the activated carbon demonstrates two broad diffraction peaks at $2\theta = 24.6^\circ$ and 43.1°, matching the diffraction of (002) and (100), respectively, signifying the formation of an amorphous structure with a defectively ordered graphite-like material [39]. The XRD patterns of the ferrite samples, prepared under different conditions show good crystallinity with well-defined peaks. The observed peaks are assigned to (111) at 18.19, (220) at 30.31°, (311) at 35.71°, (222) at 37.19°, (400) at 43.29°, (422) at 53.79°, (511) at 57.41°, and (440) at 63.01° planes revealing the formation of cubic spinel structure and correspond perfectly with the standard JCPDS data (Card No. 10–0325). The XRD of the AAC@NiF_f composite sample demonstrates peaks corresponding to the typical diffraction peaks of the NiF_f sample, besides peaks appearing at 24.6° and 43.1 matches with the planes of AAC confirming its existence in the composite sample.

The average crystallite size, D'_{XRD}, for all studied samples is calculated from the main diffraction peak by the Debye–Scherrer formula (Eq. (1)) [40]:

$$D_{XRD} = 0.9\lambda / \beta \cos\theta \quad (1)$$

where λ is the X-ray wavelength used, and β is the half-peak width of the diffraction peak. The outcomes obtained are given in Table 1, which shows that the crystallite sizes of the ferrite samples depend on the preparation method and sit in the nanometer scale range.

3.2. FT-IR

Fig. 2 demonstrates the FT-IR spectra of the investigated samples recording in the range 4000 to 400 cm^{-1}, which supports the approval of the synthesis of spinel structure. The spectra show two prominent absorption bands below 1000 cm^{-1}, a familiar characteristic of the spinel ferrites. The higher

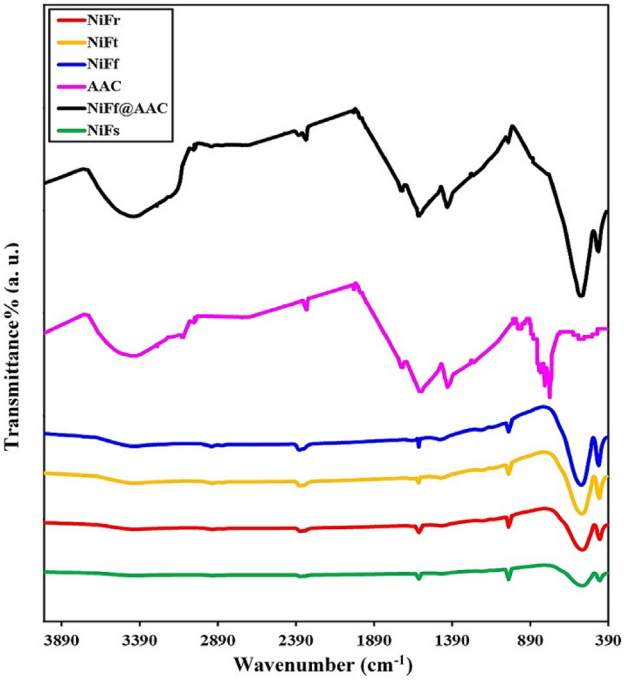

Fig. 2 – FT-IR of the investigated samples.

wavenumber band (ν_t) lies in the range 556.2–563.9 cm^{-1}, Table 1, produced by the stretching vibrations of the tetrahedral metal–oxygen bond. While the lower wavenumber band (ν_o) lies in the range 444.3–453.1 cm^{-1} and is caused by the octahedral sites' metal–oxygen vibrations [41]. The observed absorption bands are slightly different depending on the variations of synthetic methods. It may be recognized to the variation in ion distribution between tetrahedral and octahedral sites with the variation in the morphological structure. The inverse spinel nickel ferrite exhibits some Fe^{3+} ions occupying tetrahedral voids. This can be seen from the obtained spectra, which show a band at 1027 cm^{-1} credited to the stretching of Fe^{3+} and O^{2-}. The observed spectra also show bands at ~2360 and 1600 $cm^{-1,}$ assigned to H–O stretching and bending vibrational modes of free or absorbed water [42].

FT-IR spectrum of the AAC sample demonstrated three major absorption bands at 1413, 1583, and 1711 cm^{-1} besides a broad absorption peak at 3400 cm^{-1}, which is attributed to the O–H stretching vibration due to the existence of free hydroxyl groups on the carbon surface [43]. The peak observed at 1711 cm^{-1} corresponds to carbonyl C=O stretching vibration in aldehydes, ester or ketones, and carboxyl group [44]. Moreover, the absorption peak that appeared at 1583 cm^{-1} is due to C=C stretching vibrations in the aromatic ring present in the AAC sample [45]. The observed band at 1413 cm^{-1} is assigned to the bending vibrations of the C–H group present in alkyl groups [46]. The bands observed at 876 - 761 cm^{-1} are attributed to the out-of-plane bending vibrations of the C–H group in the aromatic rings [47]. Generally, the FTIR spectra of the AAC sample refer to oxygen-containing surface functional groups such as O–H, C=O, and COO groups. The spectrum of the AAC@NiF_f sample shows the most peaks observed in both AAC and NiF_f samples with shifts in the absorption bands of tetrahedral

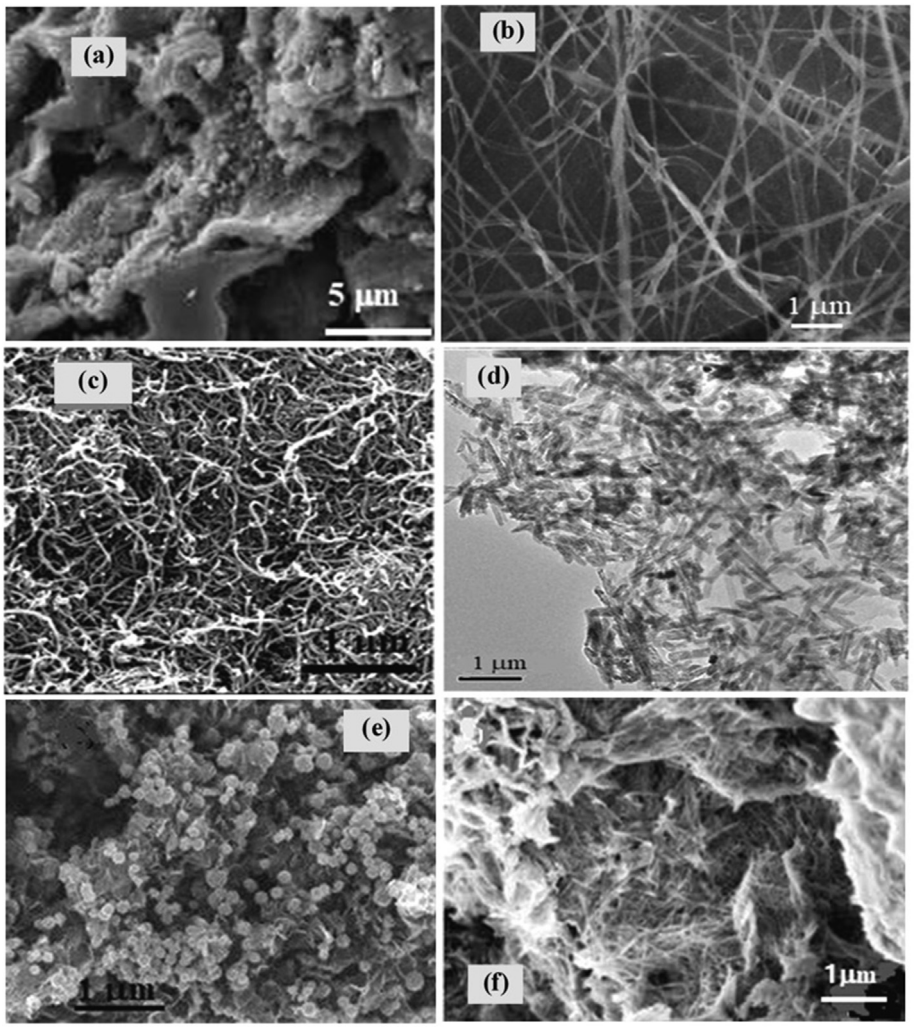

Fig. 3 – SEM micrographs for (a) AAC; (b) NiF_f; (c) NiF_t; (d) NiF_r; (e) NiF_s, and (f) AAC@NiF_f.

and octahedral groups of NiF_f and the carbonyl group of AAC. This refers to the presence of some interactions occurring between NiF_f and AAC.

3.3. *Morphological structures*

SEM and TEM techniques examined the prepared single and binary composite samples' morphological structures and the micrographs shown in Figs. 3 and 4, respectively. The SEM micrographs of the AAC sample (Fig. 3a) and TEM (Fig. 4a) show plates with a flake-like structure containing fibers with diameters of 1 nm. The SEM and TEM micrographs of NiF_f (Figs. 3b and 4b) illustrate nanofibers with an average diameter of 55 nm with a length of several millimeters. The photographs of NiF_t (Figs. 3c and 4c) show a morphology with a nanotube structure with an average pore diameter of 9 nm and length of 230 nm. The micrographs of NiF_r (Figs. 3d and 4d) show rod structure with an average diameter of 30 nm and length of 150 nm. The micrographs of NiF_s (3e and 4e) demonstrate particles with a spherical structure with an average diameter of 35 nm. The photographs of the AAC@NiF_f composite (Figs. 3f and 4f) show the mixing morphology of the constituent materials accompanied by a considerable reduction in the fiber lengths. It could also be observed that the NiF_f fibers are covered by the AAC flat sheets.

3.4. *Surface properties (nitrogen adsorption–desorption isotherms)*

Fig. 5 shows the adsorption/desorption isotherms of N_2 for all the investigated samples. The nitrogen adsorption of AAC and AAC@NiF_f composite samples showed isothermal profiles characteristic of microporosity (type 1 according to the IUPAC classification). In contrast, all the other $NiFe_2O_4$ samples exhibit isotherm nitrogen adsorption characteristics mainly of type IV. The surface area calculated by the BET analysis was found to be: 54, 82, 115, 360, 3337, and 2670 m^2/g for NiF_s, NiF_r, NiF_t, NiF_f, AAC, and AAC@NiF_f, respectively. The pore size was calculated from the adsorption isotherms using BJH (Barrett-Joyner- Halenda) and found to be 35, 41, 49, 56, 71, and 64 Å for NiF_s, NiF_r, NiF_t, NiF_f, AAC, and AAC@NiF_f, respectively. The surface data are listed in Table 1. From this, it can be noticed that the S_{BET} of the ferrites enlarges by decreasing the crystallite size.

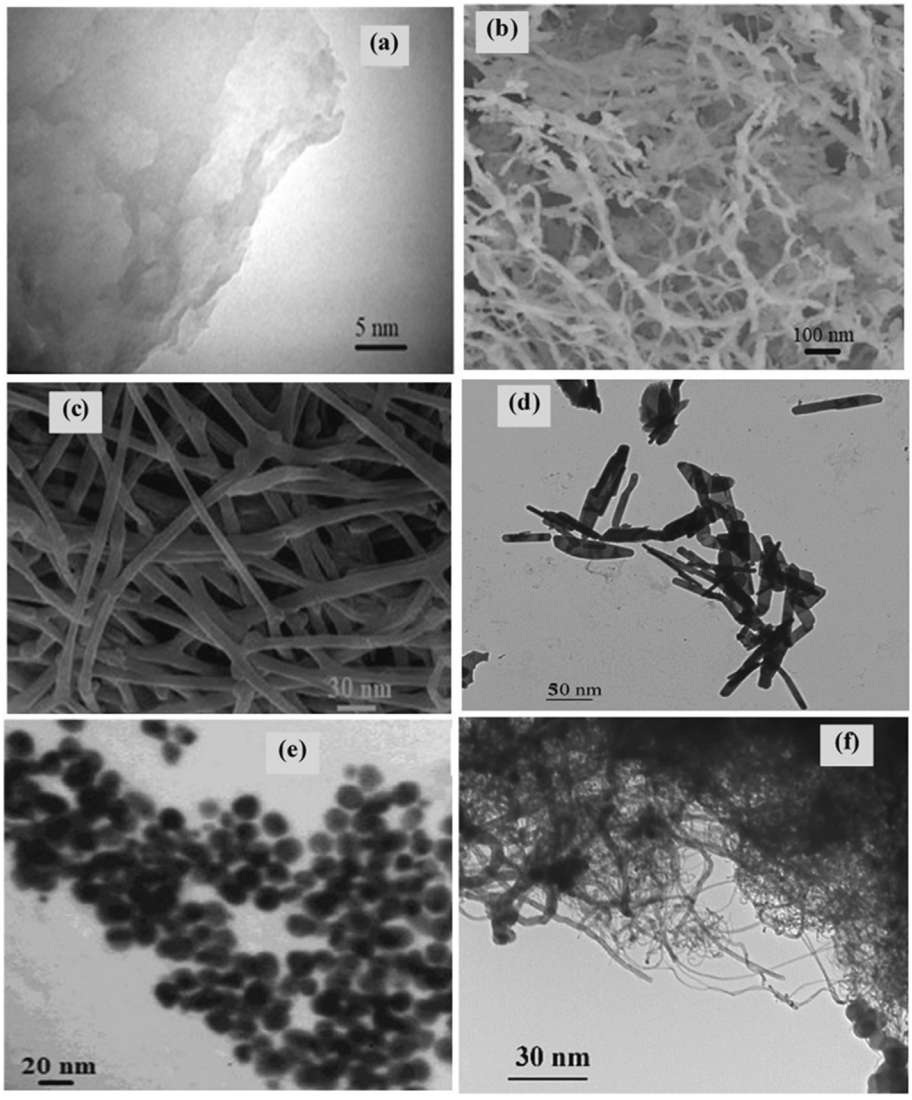

Fig. 4 – TEM micrographs for (a) AAC; (b) NiF_f; (c) NiF_t; (d) NiF_{rd}; (e) NiF_s, and (f) AAC@NiF_f.

3.5. *Electrochemical study*

3.5.1. *Single electrode*

Fig. 6 a demonstrates the cyclic voltammograms of the single-material electrode AAC, NiF_f, NiF_t, NiF_r, and NiF_s recorded in 6 M KCl electrolyte at a scan rate of 5 mV s^{-1}. The CV profile of AAC signifies the capacitive behavior with an almost semi-rectangular shape without any peaks, which is representative of the electric double-layer capacitance of carbon-based materials. In contrast, the CV curves of the NiF_2O_4 samples show a pair of sharp redox peaks, which relate to the reversible redox (charge transfer) reactions happening on the surface of the NiF_2O_4 electrodes, referring to their pseudocapacitance behavior. The major capacitance of the $NiFe_2O_4$ samples is obtained from reversible electrochemical reactions associated with [Ni/Fe] – O/[Ni/Fe] – O – OH [48]. The metal ions can undergo facile redox reactions ($Ni^{2+/3+}$and/or $Fe^{3+/2+}$) and provide pseudocapacitances [49–51] as follows:

$$NiFe_2O_4 + H_2O + 2e^- \leftrightarrow NiO + 2FeO + 2OH^- \quad (2)$$

The specific capacitance C_{sp} was evaluated from cyclic voltammograms by using Eq. (3) [52] and the results obtained are given in Table 2.

$$C_{sp} = \frac{\int idV}{2mv\Delta V} \quad (3)$$

where $\int idV$ indicates the integrated area of the CV curve while m, v, and ΔV are mass (g) of active material, potential scan rate (Vs^{-1}), and potential window (V) of the sample, respectively, the obtained results indicate that the specific capacitance follows the order: AAC@NiF_f > NiF_f > NiF_t > NiF_r > AAC > NiF_s, which goes for ferrite samples in a similar way with decreasing their particle sizes and increasing their surface areas.

Generally, the variation in pseudocapacitance of mixed transition metal oxides with their morphological structures is attributed to several factors [53–58]: Firstly, 1D nanostructures can provide more active sizes and facilitate the transfer of ions and electrons due to the nanoscale effect [53].

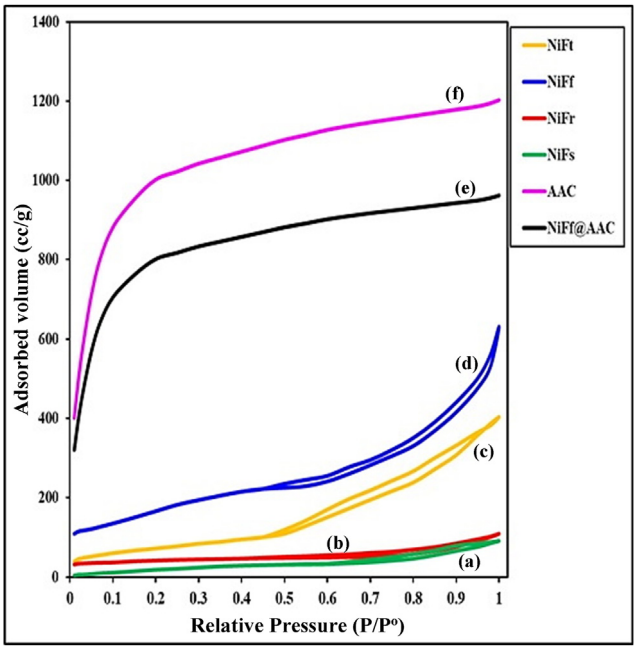

Fig. 5 – Nitrogen adsorption/desorption isotherms at 77K for (a) NiFs; (b) NiFr; (c) NiFt; (d) NiFf; (e) AAC@NiFf, and (f) AAC.

Secondly, the massive volume changes can be efficiently restrained by the 1D nanostructures. Thirdly, because of the high aspect ratio, this form of the electrode may be easily constructed into an interconnected network, facilitating its use in a flexible device [53]. All of the aforementioned factors combine to produce exceptional electrochemical features, such as high specific capacitance, high rate capability, long cycling lifespan, and possible flexible device applications [59,60].

Our results show that the NiFe2O4 nanofibers have the highest specific capacitance compared to other nanostructures (tubes, rods, and spheres) this because it has the largest surface area (NiFf (360 m2/g) > NiFt (115 m2/g) > NiFr (82 m2/g) > NiFs (54 m2/g)) which allows to store more charge or to access more active sites for the redox reaction [54]. It has the largest pore size (NiFf (5.6 nm) > NiFt (4.9 nm) > NiFr (4.1 nm) > NiFs (3.5 nm)) which facilitates ion movements into the electrode for the electrochemical reaction or screening of the external electric field [61]. It has also low charge transfer resistance from EIS data (NiFf (0.661 Ohm) < NiFt (0.665 Ohm) < NiFr (0.668 Ohm) < NiFs 0.776 Ohm)) which is attributed to its orientation characteristics in a certain direction, which effectively promotes the transport of electrons and ions. In addition, the nanowire structure shortens the distance for the de-intercalation and intercalation of K-cations [53].

The results obtained also show that the AAC electrode exhibits a high specific capacitance and demonstrated fast charge storage and transportation kinetics approved by its rectangle shape, especially at lower scan rates, Figs. 6 and 8. This refers to the that the AAC sample exhibits a pore grouping of micropores and mesopores that is appropriate for the diffusion of electrolyte ions on the electrode surface, it could participate in forming an ideal electric layer. AAC's porosity, excellent electrical conductivity, and electrolyte availability could account for the noticed high-rate capability [54]. The electrical capacitance obtained for AAC in our research at a scan rate of 1 mVs^{-1} (433 F g^{-1}) is greater than that registered by Kandasamy (94 F/g) [62], Jing (283 F/g) [63], Nor (110 F/g) [64], Daraghmeh (334 F/g) [65]. The specific capacitance values of the nickel ferrite samples are also higher than those of the previously reported values by Ghasemi (137.2 F/g) for (nanosphere particles) [12], Zate (202 F/g) for (nanosphere particles) [66]. Moreover, the composite sample, AAC@NiF_f, showed the highest capacitance in all the investigated samples due to the synergetic effect and the presence of both pseudo-capacitance and double-layers capacitance. The performance in the capacitance of the binary materials may be attached to the noticeable number of pleats present on the AAC surface, which improves the number of mesopores that can be presented to the electrolyte. Furthermore, the extraordinary conducting net offered by AAC guides development in the electron transport in the charge and discharge cycles, subsequently developing the electrical properties and charge transfer tracks formed in pure ferrite.

Galvanostatic charging–discharging (GCD) is a corresponding procedure for evaluating the C_{sp} value of electrochemical capacitors at a constant current. Fig. 6b shows the GCD curves of the investigated AAC and ferrite samples at 1 Ag^{-1} current density with a voltage between −0.1 and 0.5 V. A-like CV results; the GCD outcome also justifies the non-faradic and faradic natures of the AAC and the ferrite electrodes, respectively. The existence of a plateau at around 0.2 V in the GCD plot of the NiF_f electrode refers to the pseudocapacitive feature arising from the redox process [67].

The C_{sp} values were calculated using the following equation [68]:

$$C_{sp} = \left(\frac{i\Delta t}{m\Delta V}\right) \quad (4)$$

where i is the discharging current, Δt is the discharging time, m is the mass of the active material, and Δv is the potential range of charge and discharge [68,69]. The results acquired are given in Table 2. They agree to a large extent with those obtained from CV measurements.

The CV of the NiF_f, which exhibits the highest capacitance of the pure ferrite samples, is studied at various scan rates between 1 and 50 mV/s. The voltammograms obtained are illustrated in Fig. 6c. An ideal capacitive style is observed by the growing redox current regarding the scanning curve that also approves the reasonable rate capability of the NiF_f sample [70]. It is also noted that the currents got enlarged with rising the scan rate [71]. But, the capacitance value was reduced with increasing the scan rate due to the diffusion limitations in the pores of the electrode's surface. At the lower scan rate, the electrolyte ions can employ all the reachable sites in the active electrode material because the ions have enough time to diffuse into all the sites producing higher capacitance. On the contrary, at the high-scan rate, the electrolyte ions meet the difficulty of moving into all the available sites in the active electrode due to their restricted rate of movement in the electrolyte.

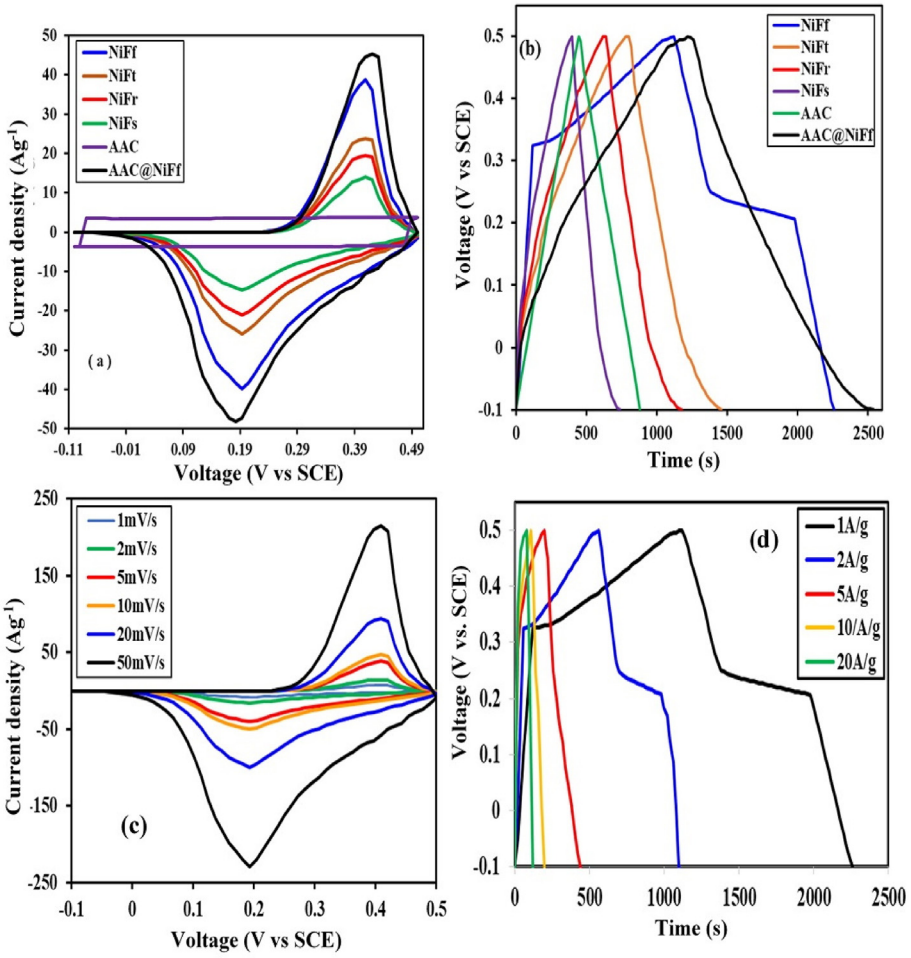

Fig. 6 – a) CV plots of the investigated single electrode in 6M KCl electrolyte solution at a scan rate of 5 mVs^{-1}. b) GCD plots of the investigated single electrodes in 6M KCl at 1A g^{-1} current density. c) CV plots of NiF_f electrode in 6M KCl electrolyte solution at different scan rates. d) GCD plots of NiF_f electrode in 6M KCl at different current densities.

The GCD technique also studied the electrochemical performance of the NiF_f electrode. The results acquired are illustrated in Fig. 6d. As opposite to AAC, the discharge curves of the NiF_f electrode show a deviation from the linearity because of its pseudocapacitive character. The C_{sp} of the electrode was calculated from the discharge cycles through Eq. (4), and the obtained results are given in Table 2, which agree well with those obtained from the CV results.

Concerning the above results, we fabricated and studied the electrochemical properties of a composite electrode composed of the NiF_f (highest pseudo capacitance electrode) and the AAC with high double-layer capacitance. The electrochemical performance of the binary composite electrode, AAC@NiF_f, was studied by CV and GCD techniques. The CV curves of the AAC@NiF_f electrode recorded in 6 M KCl electrolyte at several scan rates are represented in Fig. 7a. The figure displays a clear pair of redox peaks in each of the CV curves corresponding to the reversible redox (charge transfer) reactions occurring on the surface of the AAC@NiF_f electrode, referring to its pseudo-capacitance behavior. It is also noticed that, as expected, the current enhances by multiplying the scan rate [71,72]. The specific capacitances of the electrode were computed from the discharge cycles by applying Eq. (3). The acquired results are given in Table 2. The data obtained from GCD are represented in Fig. 7b, which shows that the discharge curves of the AAC@NiF_f electrode deviate from linearity because of its pseudocapacitive character [67]. According to Eq. (4), the specific capacitances of the electrode were calculated from the discharge cycles, and the obtained results agree well with those obtained from CV measurements, as shown in Table 2.

Electrochemical impedance spectroscopy (EIS) is essential for determining electrode materials' performance as supercapacitors. The Nyquist plot is generally generated from the data obtained from EIS measurements and is shown in Fig. 7c. For all the ferrite samples, the Nyquist plots exhibit almost straight-line behavior in the lower frequency region and semicircle behavior in the range of higher frequencies. The intersection points of the semicircles with the $Z^{/}$ axis indicate the magnitudes of the electrolyte resistance and contact resistance between the current collector and the electrodes. The semicircle refers to the charge transfer resistance (R_{ct}) at the electrode–electrolyte interface [73]. The R_{ct} – value increases in the order: NiF_s > NiF_r > NiF_t > NiF_f > AAC@NiF_f, which characterizes the order of the CT rate in the studied electrodes. The low-frequency inclined line is the feature of

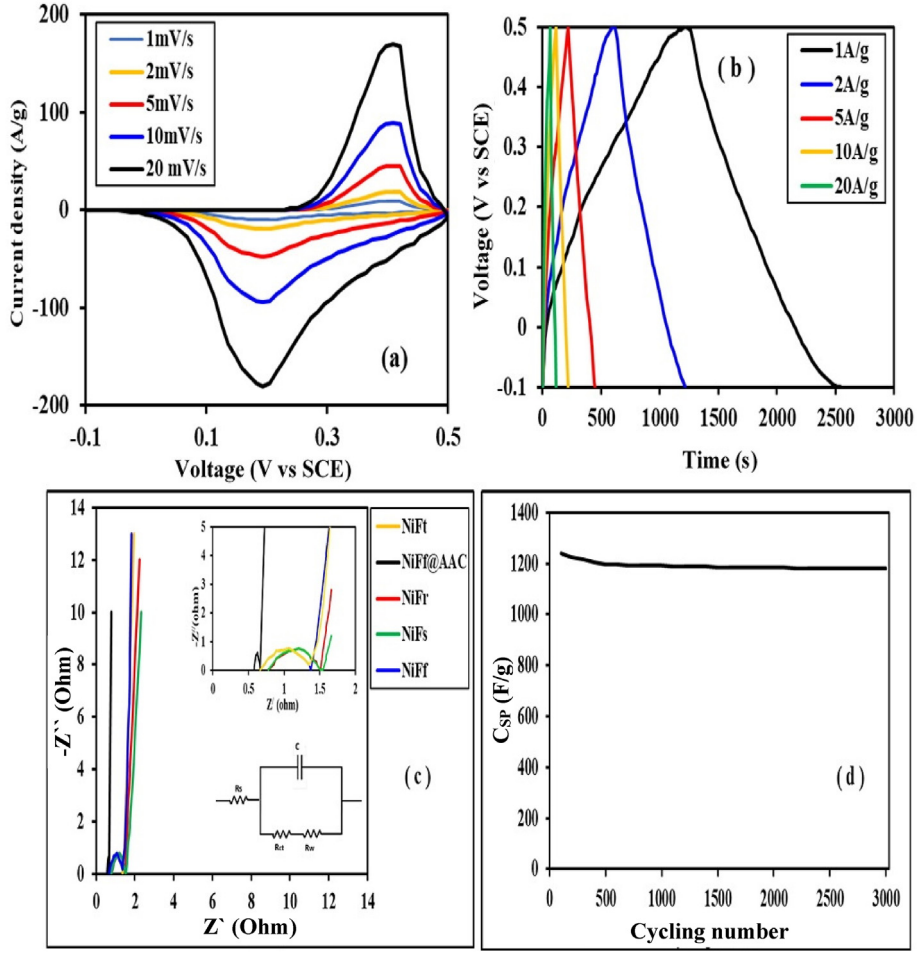

Fig. 7 – a) CV plots of AAC@NiF_f electrode in 6M KCl electrolyte solution at different scan rates. b) GCD plots of AAC@NiF_f electrode in 6M KCl at different current densities. c) Cole–Cole plots of the investigated ferrite electrodes. d) Stability of the AAC@NiF_f electrode.

the Warburg element. The slopes of the inclined lines, shown in Fig. 7c, signify the resistances that appear during the transfer of ions across the electrolyte solution to the electrode. The linear line at a lower frequency reveals the capacitive nature of the material. The slopes of the inclined lines are more perpendicular in the sequence: AAC@NiF_f > NiF_f > NiF_t > NiF_r > NiF_s, demonstrating the directive of improved capacitance performance which is consistent with the data of GCD and CV. This order can be attributed to the capabilities with which the electrolyte ions passage on a mesoporous surface of the electrode material. Accordingly, it is deduced that the AAC@NiF_f backed the charge transference and ion diffusion owing to improving the electrical conductivity and increasing the tunnels upset by AAC and the cooperation of Ni and Fe atoms. The Nyquist plots in Fig. 7c were represented by the equivalent circuit illustrated in the inset of Fig. 7c that

Table 2 – Specific capacitance values of AAC, $NiFe_2O_4$ electrodes in 6 M KCl at different CV scan rates and different discharging current densities.

	P.S[a] (nm)	C_{sp} (F g^{-1}) at different scan rates (mV s^{-1})						C_{sp} (F g^{-1}) at different I_d (A g^{-1})				
Sample		1	2	5	10	20	50	1	2	5	10	20
AAC	45	433	427	424	419	414		432	428	412	400	390
NiF_f	20	1160	1150	1140	1090	1010	960	1130	1120	1100	900	800
NiFt	33			680				660				
NiFr	41			550				520				
NiF_s	50			385				340				
AAC@NiF_f	15	1390	1330	1283	1210	1170		1260	1200	1125	1050	1000

[a] P.S is size the particle size obtained from XRD (D_{XRD}).

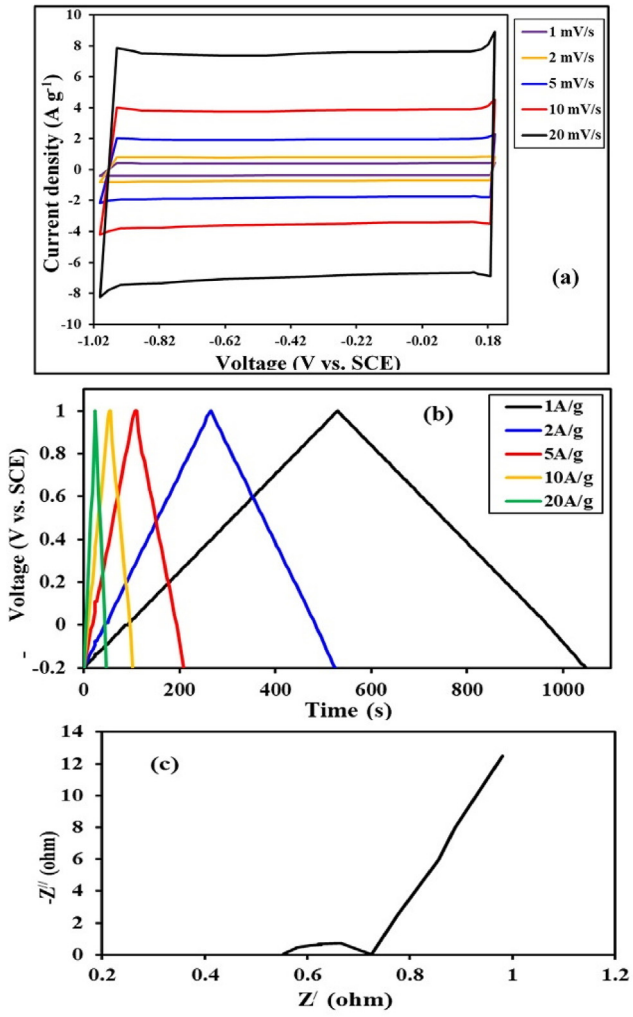

Fig. 8 – a) CV plots of AAC electrode in 6M KCl electrolyte solution at different scan rates. b) GCD plots of AAC electrode in 6M KCl at different current densities. c) Cole–Cole plots of AAC electrode in 6M KCl.

comprises R_s (contact resistance), R_{ct} (charge transfer resistance), W (Warburg impedance), and C (constant phase element). The acquired fitting parameters are given in Table 3.

The stability of the AAC@NiF_f electrode, which has the highest capacitance of all electrodes, was studied for 3000 cycles at a current density of 1 A g^{-1} and is demonstrated in Fig. 7d. It reveals a loss in C_{sp}-value of about 8% after 3000 cycles. The high stability of the AAC@NiF_f electrode could be linked to the synergistic impressions amongst the constituent materials of the binary composite. This might be attached to the fact that the AAC progresses some mechanical distortion throughout the redox process of NiF_f particles to become further stable by AAC, which works like a protective layer; all of these collectively provide for increasing the electrochemical stability.

3.5.2. *Electrochemical study of the negative electrode*

The CV voltammogram of the as-prepared AAC electrode at various scan rates (1–20 mV s-1, Fig. 8a) and the GCD cycles at several current densities (1–20 A g-1, Fig. 8b) show almost rectangular and isosceles triangular shapes, respectively, demonstrating their predominantly electric double-layer behavior [74,75]. The Csp values were evaluated by applying Eqs. (3) and (4), and viewing values lie between 390 and 433 F g-1, Table 2. The acquired results showed that the specific capacitance decreases with rising scan rates and the applied current density. This could be attributed to the accumulation and restacking of AAC layers.

Electrical impedance spectroscopy (EIS) was also performed to study the electrochemical properties of the AAC electrode. The Nyquist plot was carried out by managing ac impedance measurements at a frequency range between 10^{-1} and 10^5 Hz. Fig. 8c shows the Nyquist plot of AAC electrode in 6 M KCl aqueous solution. The inclined line observed in the low-frequency region illustrates the dominance of capacitive performance due to the development of electrical charges of the electric double-layer at the surface of the electrode. At this frequency section, the electrolyte ions can simply disperse into the mesopores of the activated carbon. The small loop area observed in the high-frequency range, Fig. 8c, characterizes the domineering resistive description of the supercapacitor system comprising of electrode/electrolyte/current collector. As mentioned above, the arc's starting denotes the R_s value ($R_s = 0.554\ \Omega$), and the arc's termination is the electrode's internal resistance ($Rp = 0.725\ \Omega$). The diameter of the arc is equal to 0.171 Ω and signifies the ESR value.

3.5.3. *Asymmetric supercapacitors*

To evaluate the applicability of the AAC@NiF_f, which exhibits the highest specific capacitance of all the examined electrodes, in the energy storage system, an asymmetric supercapacitor was made using the AAC@NiF_f as the anode electrode, and the AAC as the cathode electrode and PVA–KOH as gelled electrolyte. In this system, the AAC@NiF_f electrode has redox behavior holding a considerable pseudocapacitance value, which is valuable for amplifying the energy density of the asymmetric cell. In contrast, the AAC electrode demonstrates a large pore size and high surface area, which can gather charges during an electrostatic adsorbing–desorbing mode on the electrode surface. This is helpful for the fast introduction and pulling out the electrolyte ions for improving the cell's power density.

Inspection of the CV voltammograms of the AAC@NiF_f and the AAC electrodes in Figs. 7a and 8a show that the potential difference between the two electrodes is 1. 5 V, which is the sum of the voltage range of the positive and negative electrodes. Accordingly, the assembled asymmetric supercapacitor AAC@NiF_f//AAC could work over a voltage window between 0 and 1.5 V. Moreover, to realize the best electrochemical performance of ASC, the charge balance should be

Table 3 – Parameters values from the fitted impedance equivalent circuit of the investigated electrodes.

Sample	NiF_r	NiFs	NiF_t	NiF_f	AAC	AAC@NiF_f
R_s (Ω)	0.668	0.776	0.665	0.661	0.551	0.554
R_{ct} (Ω)	0.705	0.734	0.701	0.685	0.171	0.171
W (Ω	1.38	1.53	1.401	1.35	0.731	0.725
CPE	0.16	0.14	0.19	0.24	0.09	0.26

equal, i.e. $q^+ = q^-$. It means that the loading mass of the positive (m^+) and negative (n^-) electrodes should be assessed. This can be done by using the following equation [76,77]:

$$\frac{m^+}{m^-} = \frac{c^-}{c^+} \times \frac{\Delta V^-}{\Delta V^-} \quad (5)$$

where and $\frac{\Delta V^-}{\Delta V^-}$ are the ratios of the loading mass, the specific capacitance, and the potential windows for the cathode (+)/anode (–), respectively. The loading mass ratio $\frac{m^+}{m^-}$ was calculated to be 0.69.

The CV of the AAC@NiF$_f$//AAC Asymmetric cell (in a 1.5V window in a two-electrode configuration and electrolyte membrane composed of PVA and KOH) was measured at several scan rates between 1 and 50 mVs^{-1}. Fig. 9a shows a non-rectangular shape with a pair of redox peaks in each voltammogram, demonstrating that the charge-storage mechanism is essentially Faradaic-type owing to the redox reaction of AAC@NiF$_f$. Moreover, all CV curves did not show any change in anode and cathode peaks even at a high scan rate of 50 mVs^{-1}, signifying ideal capacitive behavior and appropriate speedy charge/discharge property for power devices.

The specific capacitance of the asymmetric cell (C_{cell}) is computed from a CV voltammogram through Eq. (6) [73,78].

$$C_{cell} = \frac{\int_{v^-}^{v^+} I(V)dV}{2MvV} \quad (6)$$

where M is the mass of the active materials in the two electrodes, v is the scan rate, and V is the potential window. The acquired results are given in Table 4.

To assess the implementation of the asymmetric supercapacitor cell, GCD under several charging currents was examined. The obtained plots are illustrated in Fig. 9b. The nonlinearity of the GCD curves denotes the contribution from the Faradaic redox reaction, compatible with the CV results.

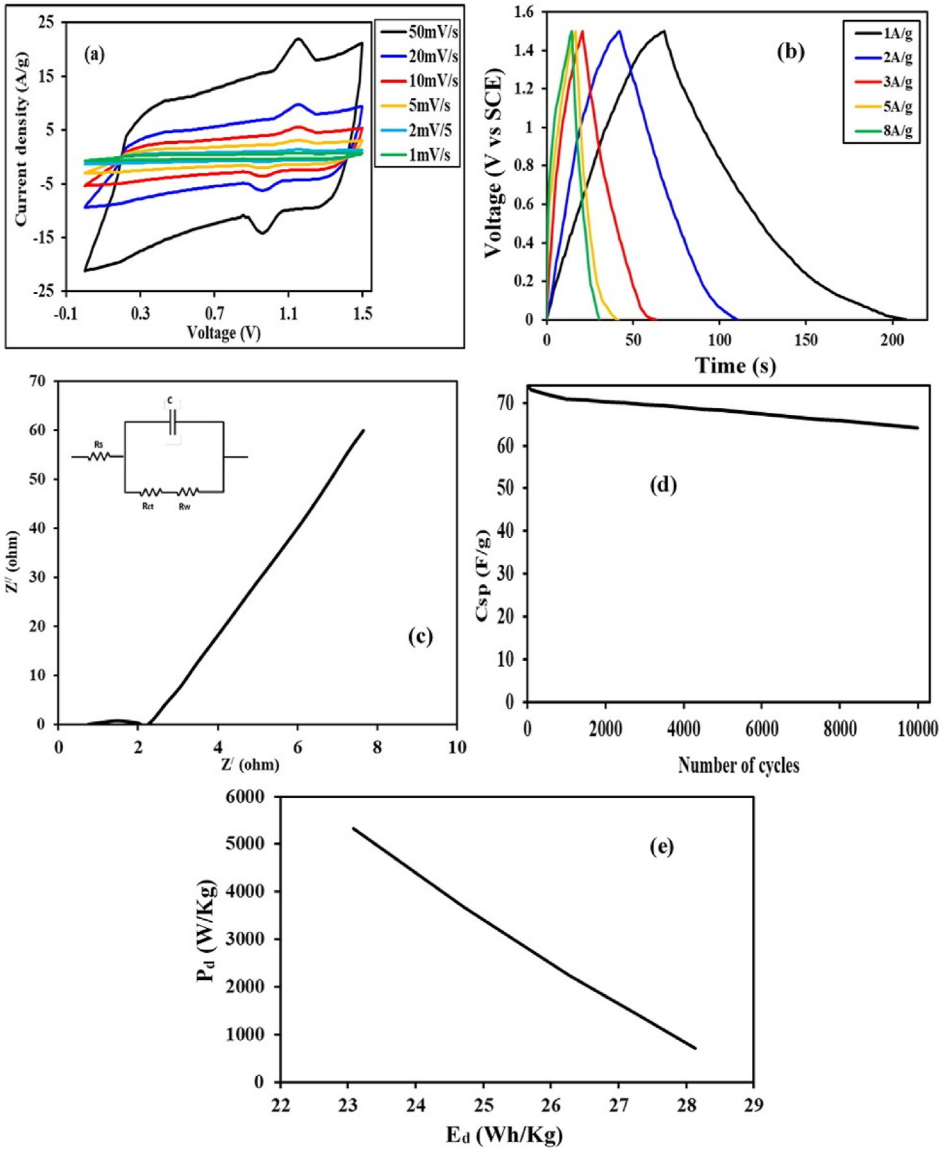

Fig. 9 – a) CV of AAC@NiFf//0AAC Asymmetric cell at different scan rates. b) GCD of AAC@NiFf//AAC asymmetric cell at different current densities. c) Cole–Cole diagram of AAC@NiFf//AAC Asymmetric cell. d) Cycling stability of AAC@NiFf//AAC Asymmetric cell. e) Ragone plot of AAC@NiFf//AAC asymmetric cell.

Table 4 – Asymmetric cell capacitance of AAC@NiF$_f$//AAC cell at several CV scan rates and various discharging current densities.

Scan rate (mV s^{-1})	C_{cell} (F g^{-1})	Current density (A g^{-1})	C_{cell} (F g^{-1})
1	95.1	1	90.0
2	92.9	2	87.2
5	89.1	3	84.1
10	85.9	5	79.1
20	84.1	8	73.9
50	77.2		

All voltammograms showed a small voltage (IR) drop, indicating evident reversibility with minor internal resistance. The specific capacitance values of the AAC@NiFf//AAC asymmetric cell are calculated grounded on the total mass of the active materials on the two electrodes from the discharge plots. The acquired outcomes are also listed in Table 4.

To review the electrical charges diffusion behavior during the charge–discharge course, the EIS of the ASC was assessed at frequencies ranging between 10^{-2} and 10^5 Hz, and the Nyquist plot is represented in Fig. 9c. The figure shows a straight line and an arc in the low and high-frequency sections, respectively, implying ideal capacitive behavior. The R_{ct} value of the sample is small and equal to 0.171 Ohm. The Nyquist plot was more examined by a simulation approach using the equivalent circuit shown in inset Fig. 9c, and the parameters gotten are listed in Table 3. The small R_{ct} value refers to a good charge-transfer conductivity of the cell at the electrolyte–electrode interface.

High cycling stability is of great importance for supercapacitor operations. Therefore, the stability of the asymmetric cell was investigated at a current density of 8 A g^{-1}, and the acquired outcomes are represented in Fig. 9d. The figure clearly illustrates that the planned AAC@NIF$_f$//AAC device shows significant cycling stability with a stable capacitance (~88% of the original capacitance) after 10000 consecutive charge–discharge cycles.

The investigated asymmetric supercapacitor device can be only feasible if it can deliver a high energy (E_d) and power (P_d) density. The two parameters were estimated at different current densities by Eqs. (7) and (8), and the obtained results are represented as Ragone plots in Fig. 9f.

$$E_d = \frac{C_{cell(\Delta V)^2}}{7.2} \tag{7}$$

$$P_d = 3600 * \frac{E_d}{\Delta t} \tag{8}$$

where C_{cell} is the cell capacitance (F g^{-1}), ΔV (V) is the voltage during the discharge process, Ed is the energy density (Wh Kg^{-1}), P_d is the power density (kW Kg^{-1}), and Δt is the discharge time (s). The results show a maximum energy density value of 28.1 Wh Kg^{-1} and a maximum density value of 5329 W kg^{-1}. These values are more significant than the comparable previously registered symmetrical systems in the literature, Table 5 [79–88].

The enhanced electrochemical performance of our asymmetric cells can be accredited for the following reasons: (1) the energy density of the supercapacitor is proportional to the square of the working voltage; therefore, enlarging the operation voltage of the asymmetric supercapacitor is a talented strategy for to increase the energy density of a supercapacitor. (2) The distinctive nanowire structure of AAC@NiF$_f$ electrode is favorable to the transfer of electrons (3) AAC has high electrical conductivity, considerable electrochemical stability, and excellent surface area. The uniformly dispersing of AAC nanosheet on the surfaces of the NiF$_f$ can efficiently raise the electroactive sites and contract the diffusion/transport ways of the electrolyte ions, causing speedy Faradaic redox processes. This guarantees an excellent rate ability at high charge/discharge rates. (4) The porous structure can appreciably develop the approachability of electrolyte ions to the electroactive electrode and simplify the fast penetration and transportation of electrolyte ions, which is helpful for high power output and rate performing at high charge/discharge rates. (5) Due to their high electrical conductivity, AAC nanosheets can work as an excellent conductive frame to encourage fast charge transfer and efficiently lessen the volume variation throughout the long-term cycling route, guaranteeing remarkable cycling stability. All these reasons permit superior charge spread dynamics, rapid electron transport, high stability, and small internal resistance of the electrodes, which subsequently improve electrochemical performance. In a few words, the synergistic involvement of electrical double-layer capacitance from AAC and pseudocapacitance from AAC@NiF$_f$ manage to superior electrochemical performance. Moreover, the acquired results confirmed that the AAC@NiF$_f$//AAC cell could instantaneously realize the high E_d of AAC@NiF$_f$ as a battery-type Faradic electrode and the high P_d of AAC as a capacitor-type electrode. Such AAC@NiF$_f$ hybrid structure displays guarantee convenient energy storage applications due to its safety and low cost.

Table 5 – A comparison between electrochemical data of some asymmetric supercapacitors configuration found in literature and the data of the present work.

Material	E_d (Wh kg^{-1})	P_d (W kg^{-1})	Ref.
$CoFe_2O_4$@C//AC	6.53	5760	[79]
$MnWO_4$//AC	12.5	550	[80]
$CoFe_2O_4$//AC	22.9	1026	[81]
NiS@AC//AC	45.6	510	[82]
CoS//AC	5.3	1800	[83]
NiO//AC	52.4	800	[84]
Co_2VO_4//AC	25.3	801	[85]
$Na_6V_{10}O_{28}$//AC	73.0	312	[86]
$CuCo_2S_4$//NG	32.7	794	[87]
$La_{0.3}$ $Sr_{0.7}$ CoO_3//AC	27.7	500	[88]
AAC@NiFe$_2$O$_4$(fiber)//AAC	23.1	5329	This work

Note: NG is nitrogen-doped graphene.

4. Conclusion

In summary, activated carbon (AAC), $NiFe_2O_4$ with different morphological structures (nanorods; NiF$_r$, nanofibers; NiF$_f$, nanotubes; NiF$_t$, and nanospheres, NiF$_s$) and binary AAC@NiF$_f$ nanocomposite are synthesized, characterized, and studied as

promise materials for supercapacitor electrodes. The crystalline phases, the morphologies, and the surface areas were examined by XRD, SEM, TEM, and BET techniques. The results showed that the prepared materials are shaped in different morphological structures with mesoporous structures. In the AAC@NiF_f composite sample, the AAC works as the platform for distributing NiF_f nanofibers, and the ferrite operates as the part to avoid AAC plates from stacking. Such a binary composite material exhibits a structure and an excellent surface area in which the diffusion of the electrolyte ions is improved and supports great diffusive charge storage. The electrical capacitance of the AAC@NiF_f electrode is higher than that found for its components. It exhibits a C_{sp} value of 1260 F g^{-1} at the current density of 1 A g^{-1} and is stable up to 3000 cycles with a loss of 8% of the initial capacitance. Asymmetric supercapacitor comprising AAC@NiF_f composite as a positive electrode and activated carbon (AAC) as a negative electrode was fabricated and investigated its electrochemical behavior. The cell showed a capacitance value of 90 F g^{-1} at a charging current density of 1 A g^{-1}. It supplied a high energy and power density of 23.1 Wh kg^{-1} and 5329 W kg^{-1}, respectively, with significant cycle stability (88% capacitance retention after 10000 cycles). The results showed that the morphological structure has a large effect on the charge storing in electrode materials and the binary AAC@NiF_f nanocomposite (cheap material) with porous structure is hopeful for energy storage devices.

Declaration of Competing Interest

The authors declare that they have no known competing financial interests or personal relationships that could have appeared to influence the work reported in this paper.

Acknowledgments

The authors extend their appreciation to the Deputyship for Research& Innovation, Ministry of Education in Saudi Arabia, for funding this research work through project number 510.

REFERENCES

[1] Majzlíková P, Sedláček J, Prášek J, Pekárek J, Svatoš V, Bannov AG, et al. Sensing properties of multiwalled carbon nanotubes grown in MW plasma torch: electronic and electrochemical behavior, gas sensing, field emission, IR absorption. Sensors 2015;15:2644–61.
[2] Maglia F, Tredici IG, Tamburini UA. Densification and properties of bulk nanocrystalline functional ceramics with grain size below 50 nm. J Eur Ceram Soc 2013;33:1045–66.
[3] Kim DH. Effects of phase and morphology on the electrochromic performance of tungsten oxide nano-urchins. Sol Energy Mater Sol Cells 2012;107:81–6.
[4] Jiang SP. Nanoscale and nano-structured electrodes of solid oxide fuel cells by infiltration: advances and challenges. Int J Hydrogen Energy 2012;37:449–70.
[5] Jeevanandam J, Barhoum A, Chan YS, Dufresne A, Danquah MK. Review on nanoparticles and nanostructured materials: history, sources, toxicity and regulations. Beilstein J Nanotechnol 2018;9:1050–74.
[6] Khan I, Saeed K, Khan I. Nanoparticles: properties, applications and toxicities. Arab J Chem 2019;12:908–31.
[7] Libich J, Máca J, Vondrák J, Čech O, Sedlaříková M. Supercapacitors: properties and applications. J Energy Storage 2018;17:224–7.
[8] Yadav HM, Ghodake GS, Kim DY, Ramesh S, Maile NC, Lee DS, et al. Nanorods to hexagonal nanosheets of CuO-doped manganese oxide nanostructures for higher electrochemical supercapacitor performance. Colloids Surf B Biointerfaces 2019;184:110500.
[9] El-Shahat M, Mochtar M, Rashad MM, Mousa MA. Single and ternary nanocomposite electrodes of Mn_3O_4/TiO_2/rGO for supercapacitors. J Solid State Electrochem 2021;25:803–19.
[10] Kumar R, Soam A, Dusane RO, Bhargava P. Sucrose derived carbon coated silicon nanowires for supercapacitor application. J Mater Sci Mater Electron 2018;29:1947–54.
[11] Sarkar A, Singh AK, Sarkar D, Khan GG, Mandal K. Three-dimensional nanoarchitecture of BiFeO3 anchored TiO2 nanotube Arrays for electrochemical energy storage and solar energy conversion. ACS Sustainable Chem Eng 2015;3:2254–63.
[12] Ghasemi A, Kheirmand M, Heli H. Synthesis of novel $NiFe_2O_4$ nanospheres for high performance pseudocapacitor applications. Russ J Electrochem 2019;55:341–9.
[13] Candelaria SL, Shao Y, Zhou W, Li X, Xiao J, Zhang J-G, et al. Nanostructured carbon for energy storage and conversion. Nano Energy 2012;1:195–220.
[14] Kumar R, Soam A, Sahajwalla V. Carbon coated cobalt oxide (CC-CO_3O_4) as electrode material for supercapacitor applications. Mater Adv 2021;2:2918–23.
[15] Kumar R, Singh BK, Soam A, Parida S, Bhargava P. In-situ carbon coated manganese oxide nanorods (ISCC-MnO_2NRs) as an electrode material for supercapacitors. Diam Relat Mater 2019;94:110–7.
[16] Mousa MA, Khairy M, Shehab M. Nanostructured ferrite/graphene/polyaniline using for supercapacitor to enhance the capacitive behavior. J Solid State Electrochem 2017;21:995–1005.
[17] Wang Y, Ding Y, Guo X, Yu G. Conductive polymers for stretchable supercapacitors. Nano Res 2018;12:1978–87.
[18] Yao X, Kong J, Zhou D, Zhao C, Zhou R, Lu X. Mesoporous zinc ferrite/graphene composites: towards ultra-fast and stable anode for lithium-ion batteries. Carbon 2014;79:493–9.
[19] Venkatachalam V, Jayavel R. Novel synthesis of Ni-ferrite ($NiFe_2O_4$) electrode material for supercapacitor applications. AIP Conf Proc 2015;1665:140016.
[20] Shinde PV, Shinde NM, Mane RS, Kim KH. Chapter 5 - ferrites for electrochemical supercapacitors. Elsevier; 2020. p. 83–122.
[21] Soam A, Kumar R, Thatoi D, Singh M. Electrochemical performance and working voltage optimization of nickel ferrite/graphene composite based supercapacitor. J Inorg Organomet Polym Mater 2020;30:3325–31.
[22] Kuo S-L, Wu N-L. Study on ferrites for supercapacitor application. 56th Annu Meet Int Soc Electrochem 2015:1–5.
[23] Anwar S, Muthu KS, Ganesh V, Lakshminarasimhan N. A comparative study of electrochemical capacitive behavior of $NiFe_2O_4$ synthesized by different routes. J Electrochem Soc 2011;158:A976.
[24] Kumar N, Kumar A, Huang GM, Wu WW, Tseng TY. Facile synthesis of mesoporous NiFe2O4/CNTs nanocomposite cathode material for high-performance asymmetric pseudocapacitors. Appl Surf Sci 2018;433:1100–12.

[25] Yu ZY, Chen LF, Yu SH. Growth of $NiFe_2O_4$ nanoparticles on carbon cloth for high-performance flexible supercapacitors. J Mater Chem 2014;2:10889–94.
[26] Javed MS, Zhang C, Chen L, Xi Y, Hu C. Hierarchical mesoporous $NiFe_2O_4$ nanocone forest directly growing on carbon textile for high-performance flexible supercapacitors. J Mater Chem 2016;4:8851–9.
[27] Senthilkumar B, Selvan RK, Vinothbabu P, Perelshtein I, Gedanken A. Structural, magnetic, electrical, and electrochemical properties of $NiFe_2O_4$ synthesized by the molten salt technique. Mater Chem Phys 2011;130:285–92.
[28] Zabotto FL, Gualdi AJ, Eiras JA, de Oliveira AJA, Garcia D. Influence of the sintering temperature on the magnetic and electric properties of $NiFe_2O_4$ ferrites. Mater Res 2012;15:428–33.
[29] Soam A, Kumar R, Sahoo PK, Mahender C, Kumar B, Arya N, et al. Synthesis of nickel ferrite nanoparticles supported on graphene nanosheets as composite electrodes for high performance supercapacitor. ChemistrySelect 2019;4:9952–8.
[30] Dujearic-Stephane K, Gupta M, Kumar A, Sharma V, Pandit S, Bocchetta P, et al. The effect of modifications of activated carbon materials on the capacitive performance: surface, microstructure, and wettability. J. Compos. Sci. 2021;5:66.
[31] Ren J, Xu Q, Li YG. Flexible fiber-shaped energy storage devices: principles, progress, applications and challenges. Flex Print Electron 2018;3:013001.
[32] Chen C, Fan Y, Gu J, Wu L, Passerini S, Mai L. One-dimensional nanomaterials for energy storage. J Phys D Appl Phys 2018;51:113002.
[33] Tan J, Zhang W, Xia A-L. Facile synthesis of inverse spinel $NiFe_2O_4$ nanocrystals and their superparamagnetic properties. Mater Res 2013;16:237–41.
[34] Selima SS, Khairy M, Bayoumy WA, Mousa MA. Influence of preparation method on structural, optical, magnetic, and adsorption properties of nano-$NiFe_2O_4$. Environ Sci Pollut Res 2019;26:21484–94.
[35] Buczek B. Preparation of active carbon by additional activation with potassium hydroxide and characterization of their properties. Adv Mater Sci Eng Article ID 2016;5819208:4.
[36] Wang J, Yang G, Wang L, Yan W. Synthesis of one-dimensional $NiFe_2O_4$ nanostructures: tunable morphology and high-performance anode materials for Li ion batteries. J Mater Chem 2016;4:8620–9.
[37] Lafta SH. Effect of pH on structural, magnetic and FMR properties of hydrothermally prepared nano Ni ferrite. Open Chem 2017;15:53–60.
[38] Kulkarni GD, Patade SR, Parlikar RR, Gopale Chilwar RR, Saraf TS, Jadhav KM. Green synthesis of $NiFe_2O_4$ nanoparticles using different fuels and their structural characterization. J Phys: Conf Ser 2020;1644:012003.
[39] Alam S, Sharma N, Kumar L. Synthesis of graphene oxide (GO) by modified hummers method and its thermal reduction to obtain reduced graphene oxide (rGO). Graphene 2017;6:1–18.
[40] Qiu S, Kalita S. Synthesis, processing and characterization of nanocrystalline titanium dioxide. Mater Sci Eng 2006;435–436:327–32.
[41] Waldron RD. Infrared spectra of ferrites. Phys Rev 1955;99:1727–35.
[42] Saikia BJ, Parthasarathy G. Fourier transform infrared spectroscopic characterization of kaolinite from Assam and Meghalaya, northeastern India. J Mod Phys 2010;1:206–10.
[43] Gonzalez JF, Silvia R, Gonzalez G, Carmen M, Nabais JM, Valente, et al. Porosity development in activated carbons prepared from walnut shells by carbon dioxide or steam Activation. Ind Eng Chem Res 2009;48:7474–81.
[44] Petrov N, Budinov T, Razvigorov M, Ekinci E, Yardim F, Minkov V. Preparation and characterization of carbon adsorbents from furfural. Carbon 2000;38:2069–75.
[45] Sricharoenchaikul V, Pechyen C, Duangdao A, Duangduen A. Preparation and characterization of activated carbon from the pyrolysis of physic nut (jatropha curcas L.). Waste, Energy Fuels 2008;22:31–7.
[46] Prasad AGD, Kumar JK, Sharanappa P. Fourier transform infrared spectroscopic study of rare and endangered medicinal plants. Rom J Biophys 2011;21:221–30.
[47] Allwar A. Characteristics of pore structures and surface chemistry of activated carbons by physisorption, ftir and boehm methods. J Appl Chem 2012;2:9–15.
[48] Kumar N, Kumar A, Huang GM, Wu W-W, Tseng TY. Facile synthesis of mesoporous $NiFe_2O_4$/CNTs nanocomposite cathode material for high-performance asymmetric pseudocapacitors. Appl Surf Sci 2018;433:1100–12.
[49] Wang Z, Zhang X, Li Y, Liu Z, Hao Z. J Mater Chem 2013;1:6393–9.
[50] Senthilkumar B, Vijaya Sankar K, Sanjeeviraja C, Kalai Selvan R. J Alloys Compd 2013;553:350–7.
[51] Shubhangi BB, Madagonda MV, Yong-Chien L, Chan J-Y, Han S-H, Anil VG, et al. Metal precursor dependent synthesis of NiFe2O4 thin films for high-performance flexible symmetric supercapacitor. ACS Appl Energy Mater 2018;1:638–48.
[52] Bindu K, Sridharan K, Ajith KM, Lim HN, Nagaraja HS. Microwave assisted growth of stannous ferrite microcubes as electrodes for potentiometric nonenzymatic H_2O_2 sensor and supercapacitor applications. Electrochim Acta 2016;217:139–49.
[53] Zhang BH, Liu Y, Chang Z, Yang YQ, Wen ZB, Wua YP, et al. Nanowire $Na_{0.35}MnO_2$ from a hydrothermal method as a cathode material for aqueous asymmetric supercapacitors. J Power Sources 2014;253:98–103.
[54] Abdel Maksoud MIA, Ramy AF, Ahmed ES, Abd Elkodous M, Olojede SO, Ahmed IO, et al. Advanced materials and technologies for supercapacitors used in energy conversion and storage: a review. Environ Chem Lett 2021;19:375–439.
[55] Nie RR, Wang QL, Sun P, Wang RJ, Yuan Q, Wang XF. Pulsed laser deposition of $NiSe_2$ film on carbon nanotubes for high-performance supercapacitor. Eng Sci 2018;6:22–9.
[56] Zhang X, Li X, Sun X, Zhang X, Kang L, Zhou Y, et al. Straightforward preparation of $Na_2(TiO)SiO_4$ hollow nanotubes as anodes for ultralong cycle life lithium-ion battery. Dalton Trans 2021;50:2521–9.
[57] Sun K, Qin JY, Wang ZX, An Y, Li XF, Dong BB, et al. Polyvinyl alcohol/carbon fibers composites with tunable negative permittivity behavior. Surface Interfac 2020;21:100735.
[58] Hou CX, Liu GF, Dang F, Zhang ZD, Chen J. Effect of strontium substitution on microstructure and magnetic properties of electrospinning $BaFe_{12}O_{19}$ nanofibers. J Wuhan Univ Technol -Materials Sci Ed 2017;32:871–4.
[59] Zhang Q, Wang X, Pan Z, Sun J, Zhao J, Zhang J, et al. Wrapping aligned carbon nanotube composite sheets around vanadium nitride nanowire arrays for asymmetric coaxial fiber-shaped supercapacitors with ultrahigh energy density. Nano Lett 2017;17:2719–26.
[60] Yongpeng M, Xiubo X, Wenyue Y, Zhipeng Y, Xueqin S, Yuping Z, et al. Recent advances in transition metal oxides with different dimensions as electrodes for high-performance supercapacitors. Adv Comp Hybrid Mater 2021;4:906–24.
[61] Vijay K, Chinnasamy RM, Raheleh A, Dominique M, Sylvio I, Michael B, et al. Pseudocapacitance of mesoporous spinel-type MCo_2O_4 (M = Co, Zn, and Ni) rods fabricated by a facile solvothermal route. ACS Omega 2017;2:6003–13.

[62] Kandasamy SK, Subramanian B, Kirshnamoorthy H. Chemically treated activated carbon for supercapacitor electrode derived from starch of solanum tuberosum. J New Mater Electrochem Systems 2021;24:78–83.
[63] Jin H, Wang X, Gu Z, Hoefelmeyer JD, Muthukumarappana K, Julsona J. Graphitized activated carbon based on big bluestem as an electrode for supercapacitors. RSC Adv 2014;4:14136–42.
[64] Nor NSM, Deraman M, Suleman M, Jasni MRM, Manjunatha JG, Othman MAR, et al. Supercapacitors using binderless activated carbon monoliths electrodes consisting of a graphite additive and pre-carbonized biomass fibers. Int J Electrochem Sci 2017;12:2520–39.
[65] Daraghmeh A, Hussain S, Saadeddin I, Servera L, Xuriguera E, Cornet A, et al. A study of carbon nanofibers and active carbon as symmetric supercapacitor in aqueous electrolyte: a comparative study. Nanoscale Res Lett 2017;12:639.
[66] Zate MK, Shaikh SF, Jadhav VV, Waghmare SD, Ahn DY, Mane RS, et al. Electrochemical supercapacitive properties of sprayed nickel ferrite nanostructured thin film electrode. J Nanoengin Nanomanufactur 2014;4:93–7.
[67] Xiaoqing C, Xiaoping S, Lianbo M, Zhenyuan, Chen X, Aihua Y. Solvothermal synthesis of NiCo-layered double hydroxide nanosheets decorated on RGO sheets for high performance supercapacitor. Chem Eng J (Lausanne) 2015;268:251–9.
[68] Lei Z, Zheng C, Yanfang W, Bingwei C, Yusong Z, Weiping T, et al. Core-shell MnO_2@Fe_2O_3 nanospindles as positive electrode for aqueous supercapacitors. J Mater Chem 2015;3:22066–72.
[69] Kharade PM, Thombare JV, Babar AR, Bulakhe RN, Kulkarni SB, Salunkhe DJ. Electrodeposited nanoflakes like hydrophilic Co_3O_4 as a supercapacitor electrode. J Phys Chem Solid 2018;120:207–10.
[70] Nagamuthu S, Vijayakumar S, Muralidharan G. Synthesis of Mn_3O_4/amorphous carbon nanoparticles as electrode material for high performance supercapacitor applications. Energy Fuels 2013;27:3508–15.
[71] Selvan R, Perelshtein I, Perkas N, Gedanken A. Synthesis of hexagonal-shaped SnO_2 nanocrystals and SnO_2@C nanocomposites for electrochemical redox supercapacitors. J Phys Chem C 2008;112:1825–30.
[72] He Jianli C, Yuhang L, Xicui Z, Bin W. Thin-walled hollow fibers for flexible high energy density fiber-shaped supercapacitors Chuan Energy. Mater 2021;1:100010.
[73] Mousa MA, Khairy M, Shehab M. Nanostructured ferrite/graphene/polyaniline using for supercapacitor to enhance the capacitive behavior. J Solid State Electrochem 2017;21:995–1005.
[74] Xie LJ, Sun GH, Su FY, Guo XQ, Kong QQ, Li XM, et al. Hierarchical porous carbon microtubes derived from willow catkins for supercapacitor applications. J Mater Chem 2016;4:1637–46.
[75] Zhang F, Liu TY, Hou GH, Kou TY, Yue L, Guan R, et al. Hierarchically porous carbon foams for electric double layer capacitors. Nano Res 2016;9:2875–88.
[76] Shasha J, Tiehu L, Xiong C, Tang C, Dang A, Li H, et al. Application of zero-dimensional nanomaterials in biosensing. Nanomaterials 2019;9:1338–50.
[77] Li Chunyang, Wu Wenzhuo, Wang Peng, Zhou Weibin, Wang Jing, Chen Yuhui, et al. Fabricating an aqueous symmetric supercapacitor with a stable high working voltage of 2 V by using an alkaline–acidic electrolyte. Adv Sci 2019;6:1801665.
[78] Sun M, Tie J, Cheng G, Lin T, Peng S, Deng F, et al. In situ growth of burl-like nickel cobalt sulfide on carbon fibers as high-performance supercapacitors. Mater Chem 2015;3:1730–6.
[79] Zhao Y, Xu Y, Zeng J, Kong B, Geng X, Li D, et al. Low-crystalline mesoporous $CoFe_2O_4$/C composite with oxygen vacancies for high energy density asymmetric supercapacitors. RSC Adv 2017;7:55513–22.
[80] Donolikar PD, Patil S, Sadale SB, Ryu J, Patil DR. Redox-active electrolyte-based MnWO4//AC asymmetric supercapacitors,J Mater Sci Mater Electron 32: 8054–8063..
[81] Gao H, Xiang J, Cao Y. Hierarchically porous CoFe2O4 nanosheets supported on Ni foam with excellent electrochemical properties for asymmetric supercapacitors. Appl Surf Sci 2017;413:351–9.
[82] Cao S, Li H, Zhou X, Guo H, Chen Y. NiS/activated carbon composite derived from sodium lignosulfonate for long cycle-life asymmetric supercapacitors. J Alloys Compd 2022;900:16354.
[83] Subramani K, Sudhan N, Divya R, Sathish M. All-solid-state asymmetric supercapacitors based on cobalt hexacyanoferrate-derived CoS and activated carbon. RSC Adv 2017;7:6648–59.
[84] Vinodh R, Babu RS, Atchudan R, Kim HJ, Yi M, Samyn LM, et al. Fabrication of high-performance asymmetric supercapacitor consists of nickel oxide and activated carbon (NiO//AC). Catalysts 2022;12:375.
[85] Li Ch, Ma D, Zhu Q. ZIF-67 derived Co_2VO_4 hollow nanocubes for high-performance asymmetric supercapacitors. Nanomaterials 2022;12:848.
[86] Chen HY, Wee G, Al-Oweini R, Friedl J, Tan KS, Wang Y, et al. A polyoxovanadate as an advanced electrode material for supercapacitors. ChemPhysChem 2014;15:2162–9.
[87] Dong H, Li Y, Chai H, Cao Y, Chen X. Hydrothermal synthesis of $CuCo_2S_4$ nano-structure and N-doped graphene for high-performance aqueous asymmetric supercapacitors. ES Energy Environ 2019;4:19–26.
[88] Cao Y, Lin B, Sun Y, Yang H, Zhang X. Symmetric/asymmetric supercapacitor based on the perovskite-type lanthanum cobaltate nanofibers with Sr-substitution. Electrochim Acta 2015;178:398–406.